JAMES | Journal of Advances in Modeling Earth Systems

RESEARCH ARTICLE
10.1029/2018MS001383

A Statistical Model for Isolated Convective Precipitation Events

Christopher Moseley[1], **Olga Henneberg**[2], **and Jan O. Haerter**[2]

[1]Max Planck Institute for Meteorology, Hamburg, Germany, [2]Niels Bohr Institute, Copenhagen University, Copenhagen, Denmark

Key Points:
- We describe large eddy simulations of idealized diurnal cycles with convection
- A storm tracking algorithm for convective rain events is refined and analyzed
- A statistical model for isolated convective rain cells is proposed

Supporting Information:
- Supporting Information S1
- Figure S1
- Figure S2
- Figure S3
- Figure S4
- Figure S5
- Figure S6

Correspondence to:
C. Moseley,
christopher.moseley@mpimet.mpg.de

Citation:
Moseley, C., Henneberg, O., & Haerter, J. (2019). A statistical model for isolated convective precipitation events. *Journal of Advances in Modeling Earth Systems*, *11*, 360–375. https://doi.org/10.1029/2018MS001383

Received 24 MAY 2018
Accepted 8 JAN 2019
Accepted article online 17 JAN 2019
Published online 29 JAN 2019

Abstract We present a highly simplified model to describe the diurnal evolution of a convective cloud field in idealized large eddy simulations. The life cycles of individual precipitation events are detected by a storm tracking algorithm which records the autonomous appearance and decay, as well as the merging and fragmentation of convective precipitation cells. Conditioned on the area covered by each cell, the tracking method records the time evolution of the precipitation intensity, the anomalies of near-surface temperature and moisture, convective available potential energy, and convective inhibition. For tracks that do not merge or split (termed *solitary*), many of these quantities show generic, often nearly linear relations that hardly depend on the forcing conditions of the simulations, such as surface temperature. This finding allows us to propose a simple idealized model of precipitation events, where the surface precipitation area is circular and a cell's precipitation intensity falls off linearly with the distance from the respective cell center. The drop-off gradient is nearly independent of track duration and cell size. Multiple track properties, that is, track duration, peak, and mean intensity, as well as the associated cell area can hence be specified by knowing only one remaining parameter. In contrast to the simple and robust behavior of solitary tracks, tracks that result from merging of two or more cells show a much more complicated behavior. The most intense, long lasting, and largest tracks stem from tracks involved in repeated merging.

1. Introduction

Recent studies, using both observational and simulated data, argued that future warmer climate conditions may result in an intensification of convective precipitation (Lenderink & van Meijgaard, 2008; Lenderink et al., 2017; O'Gorman & Schneider, 2009; Westra et al., 2014), potentially increasing the risk of flood (Kendon et al., 2014). Historical high-resolution data show that convective precipitation intensities are particularly sensitive to temperature changes (Berg et al., 2013; Lenderink & van Meijgaard, 2008; Lenderink et al., 2009; Molnar et al., 2015), but the exact mechanisms causing extreme convective precipitation or its temperature dependence are, to date, not fully understood.

A recent paper suggested that disappearance of local convective inhibition (CIN) in a given location is a necessary prerequisite for the onset of convection there (Moseley et al., 2016). Negative buoyancy contributions, defined as CIN, are hence a plausible indicator of times and locations at which convection is suppressed. Convective available potential energy (CAPE) is a traditional predictor for convective intensity and updraft speed, repeatedly used in subgrid closure schemes for convective parametrization in large scale models (Arakawa, 2004; Arakawa & Schubert, 1974). Failure of convective parametrizations was found to be more likely under nonequilibrium conditions, that is, departures from the quasi-equilibrium assumption (Neelin et al., 2008). In those situations CAPE is rapidly modified with the onset of convection and not balanced by large scale processes (Done et al., 2006; Zimmer et al., 2011).

CAPE and CIN are conceptual, idealized quantities, based solely on the adiabatic ascent of a test parcel originating at a certain height above the surface but neglect the effects of mixing. Here we aim to address the interplay between CAPE, CIN, and local precipitation production as well as other thermodynamic quantities. The local thermodynamic conditions before and during the initiation of precipitation cells are influenced in three different ways: first, by surface latent and sensible heat fluxes as well as the redistribution of moisture and temperature within the boundary layer. Second, by latent heat release within the cloud that eliminates the temperature differences between the parcel and the ambient air temperature (Done et al., 2006), and third, due to mixing with the environment within the cloud. To show that the latter two play

only a minor role for local CAPE, we define CAPE and CIN as local quantities by lifting a test parcel from the lowest model level and vertically integrating its buoyancy within the local air column and alternatively versus the horizontal mean air column. However, other authors (e.g., Zimmer et al., 2011) have in contrast assumed that tropospheric heating and boundary layer cooling and drying contribute approximately equally to the reduction of CAPE.

Storm tracking algorithms have proven useful in studying the interaction of convective rain cells (Dawe & Austin, 2013). In recent years, a number of methods for the tracking of individual clouds and convective storms have been developed. These methods identify single convective cells and follow their evolution throughout the life cycle, that is, from the formation of a cell to the dissolution. Storm tracking methods have been developed for different purposes and are therefore specialized in one way or the other. Elaborate and optimized storm tracking methods in two and three dimensions have been geared toward the nowcasting of thunderstorms (Dixon & Wiener, 1993; Hering et al., 2005; Kober & Tafferner, 2009); other methods identify clouds and thermals to study the cloud statistics in shallow (Heiblum et al., 2016; Heus & Seifert, 2013) or deep convection (Senf et al., 2018; Tsai & Wu, 2017).

Our current tracking method focuses on the life cycle of convective precipitation tracks in both observed and simulated 2-D data, such as 2-D radar precipitation observation products and surface precipitation from large eddy simulations (LES) output. We build on the *Iterative Rain Cell Tracking* (IRT) originally developed for the analysis of radar data (Moseley et al., 2014). IRT is simple, but it is able to distinguish merging and fragmentation incidents and therefore caters to statistical analysis of different track types.

Mergers have been described both observationally (Byers & Braham, 1949; Simpson et al., 1980) and by computer simulations (Glenn & Krueger, 2017; Tao & Simpson, 1989), suggesting that combined cells can produce more intense precipitation and that merging can lead to larger detrainment heights (Glenn & Krueger, 2017). In IRT, instantaneous contiguous objects of precipitation are identified and checked for overlaps with the respective consecutive time steps. IRT capitalizes on the fact that, even under large scale advection, larger objects mostly overlap from one time step to the next, thereby allowing to identify tracks formed by the objects with overlap. By iterating, also smaller rain cells are captured, which often do not overlap when they are advected.

An approach similar to IRT has more recently been applied to the analysis of radar data over the Netherlands—finding that the temperature scaling of cell intensities depends on the cell size (Lochbihler et al., 2017). IRT has further been applied to precipitating convective updrafts generated by idealized LES (Moseley et al., 2014). The main finding there was that tracks resulting from the merging of previous tracks react much more strongly to forcing conditions when compared to tracks that did not interact, so-called *solitary tracks*. The reason for this insensitivity of the solitary tracks to surface forcing could not yet clearly be identified. It could be speculated that solitary tracks are mainly driven by the feedback between the boundary layer and the free atmosphere, which is largely independent of the boundary layer height.

To address the relation between CAPE, CIN, and precipitation, IRT is here extended to record also an arbitrary number of auxiliary fields by conditioning on surface precipitation intensity (section 2). We hence yield the time evolution both for the main tracking field and all auxiliary fields. In section 3 we describe our results, including overall track statistics and a characterization of the track life cycle. We then discuss the relation between CAPE, CIN, and near-surface temperature changes. Based on this relation, we propose a simple statistical model which captures the relation between cell duration, cell maximum intensity, and cell area. We finally discuss the implications and possible extensions and conclude (section 4).

2. Tracking Method and Model Simulation Data

2.1. Tracking Method

2.1.1. Objects and Tracks

The algorithm diagnoses precipitation cells, or contiguous areas defined by any other field, as disparate entities in space, in the following called *objects*. Precipitating and nonprecipitating areas are separated by a fixed threshold $I_{\min}$. Throughout this paper, we choose a fixed threshold intensity of $I_{\min} = 1$ mm/hr since this value corresponds to the typical limit of detectability in radar measurements (Moseley et al., 2014). After object identification, the tracking algorithm links objects between two consecutive output time steps when they overlap. Such overlapping objects are then considered part of the same *track*. By definition, we require an object to consist of at least four grid boxes, and a track must be at least two time steps long (i.e., tracks that

are only one time step long are neglected). We define the track *lifetime* as the number of time steps multiplied by the output interval of the input fields, for example, to a track that is six time steps long, we would assign a lifetime of 30 min, since our LES data have an output interval of 5 min. Note that the term "object" is used here for a precipitation cell at a given instant in time, while a "track" is an entity with a given lifetime, that is, it links all objects at different time steps together that belong to the same precipitation event.

2.1.2. Iteration

Under rapid advection, smaller objects often do not overlap from one time step to the next, although they might belong to the same updraft process. To remedy this shortcoming, an iterative procedure is applied: Object identification is performed once for all time steps, and a mean advection velocity field of the moving objects is diagnosed from the tracking result. Subsequently, the tracking is repeated by taking into account the diagnosed velocity field, such that each object is displaced by $\Delta r \equiv \Delta t \cdot v$, where Δr is the displacement, Δt the data output time step, and v is the diagnosed effective advection velocity. This procedure results in an improved match of any given object with the corresponding object of the consecutive time step (for details, see Moseley et al., 2014). Generally, the iterative procedure has to be repeated several times until the diagnosed velocity converges.

2.1.3. Merging and Fragmentation

The main challenge for the tracking algorithm is the handling of merging and fragmentation incidents. When very small objects combine with much larger ones, one might not consider the resulting track distinct from the larger of the two. We therefore introduce a parameter θ, termed the *termination sensitivity*, that can be used to distinguish if a merging/fragmentation incident entails the termination of all involved tracks or if the largest track is continued. Specifically, we define as follows:

- *Merging incident:* two or more objects at time step t overlap with one object at time step $t+1$. The algorithm determines the areas A_i of the largest object O_i and A_j of the second largest object O_j at time t. If $A_j/A_i < \theta$, then O_i is continued as the merged object at time $t+1$, while O_j and (if present) all other smaller objects are terminated. Otherwise, if $A_j/A_i \geq \theta$, all objects at time t are terminated, and the merged object at time $t+1$ is initiated as a new track and labeled as a track initiated from merging.
- *Fragmentation incident:* The definition is analogous but for the case where parts of one track separate from an existing track. Now the areas of the fragments are compared, again using the comparison of the largest and second to largest area, as for mergers from one time step to the next. In principle, a fragmentation incident is the time reverse of a merging incident.

The parameter θ takes values $0 \leq \theta \leq 1$. If $\theta = 0$, every merging and fragmentation incident leads to the termination of all involved tracks and to a new initiation of all resulting tracks. The main objective for the introduction if θ is the reduction of noise: If a very small object splits off or merges into a much larger one, it can be avoided that the large track is immediately terminated by such an event by choosing a nonzero value for θ. For $\theta = 1$, upon merging or fragmentation, at least the track with the largest object area at the time of the merging continues.

2.1.4. Book Keeping

Tracks are labeled by the type of their initiation and termination. We use the notation *X*-*Y*, where $X \in$ {s,m,f,a} denotes the type of initiation, that is, as a new *solitary* event (s), as a result of a *merging* event (m), or as a *fragment* of a splitting-up of another track (f), and $Y \in$ {s,m,f,a} denotes the type of termination, that is, dissolution as a solitary event (s), by merging with another track (m), or by *fragmentation* or breaking-up into other tracks (f). For instance, *s*-*s* refers to all tracks that begin and end as solitary. Tracks of type *s*-*s* thus do not interact with other tracks, while *m*-*s* denotes tracks that begin as a merging result but terminate by dissolution. The symbol *a* is used as a place holder for all of the three types s,m,f for either initiation or termination, for example, *s*-*a* refers to tracks that begin as solitary but terminate in any of the three possibilities. In the following, we will refer to tracks of type *s*-*s* simply as solitary, as they will constitute the main subject of the discussion. Note that the terms *initiation* and *termination* are used here only in association with the tracks as mathematical objects identified by the IRT algorithm and not with the physical rain events as such, which of course do not terminate when merging and fragmentation incidents take place. The number of tracks detected for each track type depends on the choice of the parameter θ, as will be discussed in section 3.1.

2.1.5. Auxiliary Variables

Area mean and maximum and minimum of any additional fields are recorded for the areas defined by the main tracking variable (here surface precipitation). Here we record the following additional variables: Anomalies, that is, subtracting the current domain mean, of temperature in the lowest model level, CAPE,

and CIN. CAPE and CIN are defined at a gridbox level using an adiabatically lifted test parcel from the surface to the level of neutral buoyancy (see section 2.3).

2.1.6. Boundary Conditions

IRT can be applied on data either with periodic (as is the case here) or open boundary conditions (such as for remote sensing data or limited area simulations). Further, IRT can also handle missing values which may occur in observational data.

2.1.7. Fortran 90 Source Code

We make the IRT program code publicly available. The source code, including a user's manual and a tutorial, can be downloaded via the URL:
https://github.com/christophermoseley/iterative_raincell_tracking.

2.2. Model Simulation Data

We simulate an idealized convective diurnal cycle using the University of California, Los Angeles LES model, including a delta four-stream radiation scheme and a two-moment cloud microphysics scheme (Stevens et al., 2005). Subgrid-scale turbulence is parametrized after Smagorinsky. The domain size is 1,024 × 1,024 grid boxes with a horizontal grid spacing of 200 m, with 75 vertical levels which stretch from a spacing of 100 m near the surface to 400 m at the model top, located at 16.5 km. The simulation is initialized by horizontally homogeneous temperature and moisture profiles. The temperature profile starts with 21 °C at the lowest model level with a lapse rate of 6.6 K/km below 11 km and 3 K/km above. The profile of relative humidity starts with 65% in the first model level, linearly increases by 12% km^{-1} below 2 km, decreases by 12.5% km^{-1} between 2 and 4 km, by 2% km^{-1} between 4 and 10 km, and by 12% km^{-1} higher up.

The diurnal cycle is imposed by a varying surface temperature (T_{surf}) profile following $T_{surf}(t) = T_0 + \Delta T \sin((t-6)\pi/12)$, where t denotes the time in units of hours after midnight, and the solar insolation at a latitude of 52° N. Surface sensible and latent heat fluxes are then computed interactively by the model using Monin-Obukhov similarity theory. T_0 is the daily average surface temperature and was varied between T_0 = 23, 25, and 27 °C, denoted in the following as the CTR, P2K, and P4K simulations, respectively. The temperature amplitude is $\Delta T = 10$K. We approximate the effect of a moist land surface by assuming a specific humidity of the surface layer to 70% of its saturation value (i.e., as it would be given over an ocean surface). An additional run, which includes large-scale advective forcing as well as a simulated vertical lifting, is denoted as *OMEGA*. For all simulations, we chose an output interval of 5 min for the full 3-D prognostic fields.

The simulation OMEGA, in contrast to CTR, P2K, and P4K, includes homogeneous large scale wind shear and is therefore qualitatively different from the simulations without shear: Precipitation objects are elongated in the flow direction and grow larger during the course of the day. The iteration process mentioned in section 2.1 is required for the OMEGA simulation only, but not for CTR, P2K, and P4K, since there is no background flow in the latter simulations. Although the focus of the following results section is on the three simulations without large scale forcing, we include OMEGA for the sake of completeness and argue that the behavior of convective events is fundamentally different in the case of wind shear and would require a special consideration.

2.3. Calculation of Local CAPE and CIN

For the calculation of CAPE and CIN, in every model column, we lift an imaginary air parcel along a pseudoadiabat, starting from the lowest model level, up to the model top. CAPE is then given by

$$CAPE = \int_{\mathrm{LFC}}^{\text{model top}} g\left(\frac{T_{v,\mathrm{parcel}} - T_v}{T_v}\right) \mathrm{d}z, \tag{1}$$

where T_v is the virtual temperature of the air in the column, $T_{v,\mathrm{parcel}}$ is the virtual temperature of the parcel, and the integral is taken over all values of z above condensation level where $T_{v,\mathrm{parcel}} > T_v$, that is, where the parcel has positive buoyancy. LFC denotes the lifted condensation level. CIN is given by

$$CIN = \int_{0}^{\mathrm{LFC}} g\left(\frac{T_v - T_{v,\mathrm{parcel}}}{T_v}\right) \mathrm{d}z, \tag{2}$$

where the integral is taken over all values of z below the level of free convection where $T_{v,\mathrm{parcel}} < T_v$, that is, where the parcel has negative buoyancy.

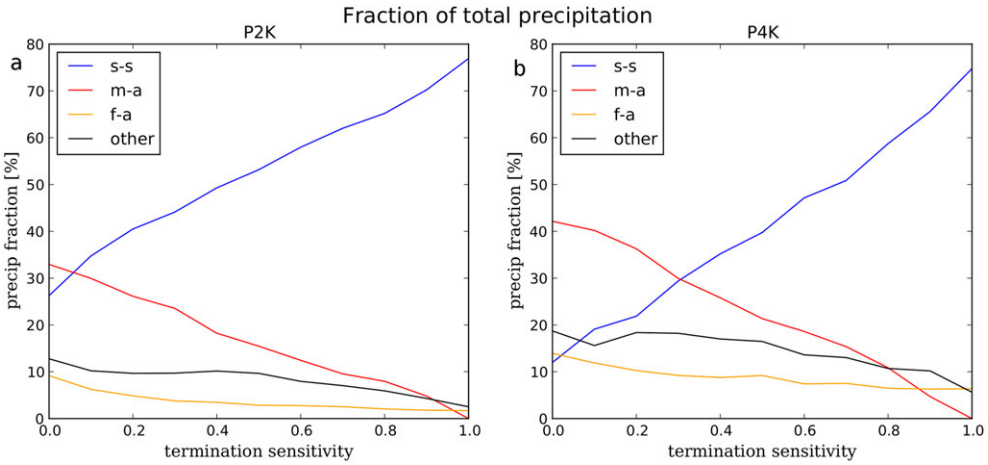

Figure 1. Fraction of total accumulated rainfall for track types *s-s* (solitary), *m-a* (mergers), *f-a* (fragments), and remaining types (*other*) versus the termination sensitivity θ, for the simulations *P2K* (a) and *P4K* (b).

We approximate the pseudoadiabat by a dry adiabat below the lifting condensation level (LCL); above the LCL, we integrate the temperature lapse rate given by Emanual (1994)

$$-\frac{\mathrm{d}T}{\mathrm{d}z} = \frac{\Gamma_d + \frac{L_v}{c_p}\frac{R_\mathrm{d}/R_\mathrm{c}\times e_\mathrm{sat} pg}{(p-0.378e_\mathrm{sat})^2 R_\mathrm{d} T}}{1 + \frac{L_v}{c_p}\left(\frac{R_\mathrm{d}/R_\mathrm{v}}{p-0.378e_\mathrm{sat}} + \frac{0.378R_\mathrm{d}/R_\mathrm{v}\times e_\mathrm{sat}}{p-0.378e_\mathrm{sat}}\right)\frac{de_\mathrm{sat}}{\mathrm{d}T}} \tag{3}$$

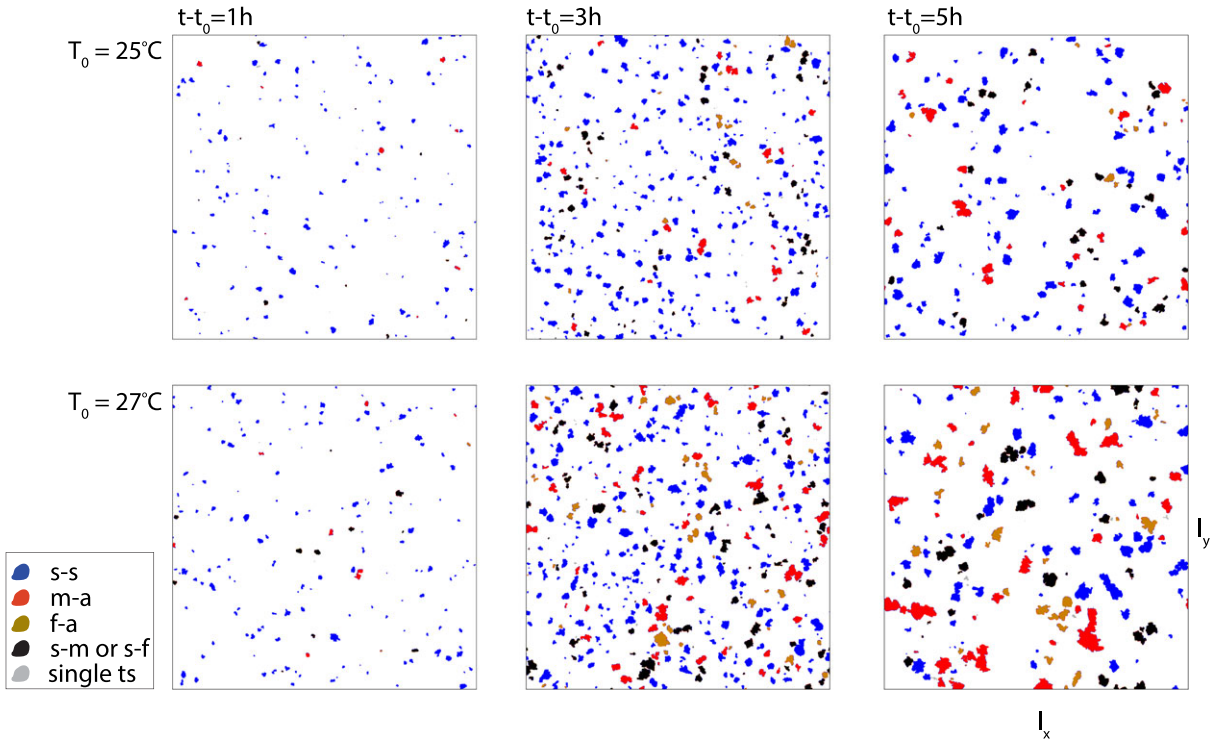

Figure 2. Time sequences of tracked objects. Precipitation objects 1, 3, and 5 hr after the onset of precipitation for $T_0 = 25$ °C (*P2K*) and $T_0 = 27$ °C (*P4K*), as labeled, with $\theta = 0.5$. Objects are colored by their track type as indicated in the legend. "single ts" labels tracks that lasted for only a single time step. $\theta = 0.5$, $l_x = l_y = 204$ km.

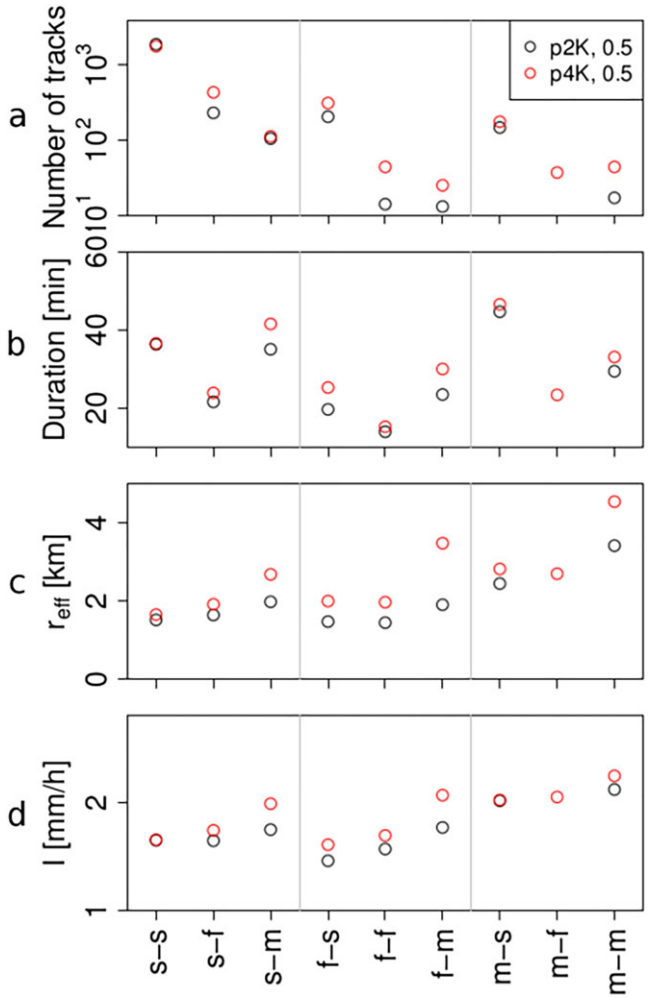

Figure 3. Relative track properties. Number of tracks (a), averages of track duration (b), effective patch radius (c), and precipitation intensity (d) for each track type. Only cases with more than 10 data points were considered in the statistics. Note the logarithmic vertical axis scale in top panel.

to obtain $T(z)$. Here R_d and R_v are the specific gas constants of dry air and water vapor, respectively, L_v is the latent heat of vaporization, c_p is the specific heat capacity of dry air at constant pressure, e_{sat} is the saturation vapor pressure with respect to liquid water, p is the air pressure, and $\Gamma_d = 9.8$ K/km is the dry adiabatic lapse rate.

3. Results

3.1. Categorization of Track Types

IRT discriminates three processes by which tracks can be initiated and terminated: solitary (s), merging (m), or fragmentation (f), hence yielding nine possible combinations. The number of tracks that are detected within each type depends on the choice of the parameter θ. To give a basic assessment of the impact of θ, we compute the total precipitation throughout the diurnal cycle for several track categories (Figure 1), that is, pure solitary (*s-s*), all tracks initiated through a merging incident (*m-a*), tracks initiated during fragmentation (*f-a*), and remaining track types (termed: *other*), that is, *s-m* or *s-f*. The sum of all components shown amounts to approximately 80% for *P2K* and 86% for *P4K*. The remaining precipitation with intensities below 1 mm/hr bypasses the object identification or belongs to tracks that are only one time step long. Lower threshold values will naturally increase the records of low-intensity precipitation objects. As Figure 1 shows, the fraction of the different categories varies substantially with θ, with the contribution of solitary tracks increasing with θ at the expense of mergers. For very low values of θ, even very small tracks can lead to such merging and fragmentation incidents which might perturb a clear signal of the interaction. Conversely, for

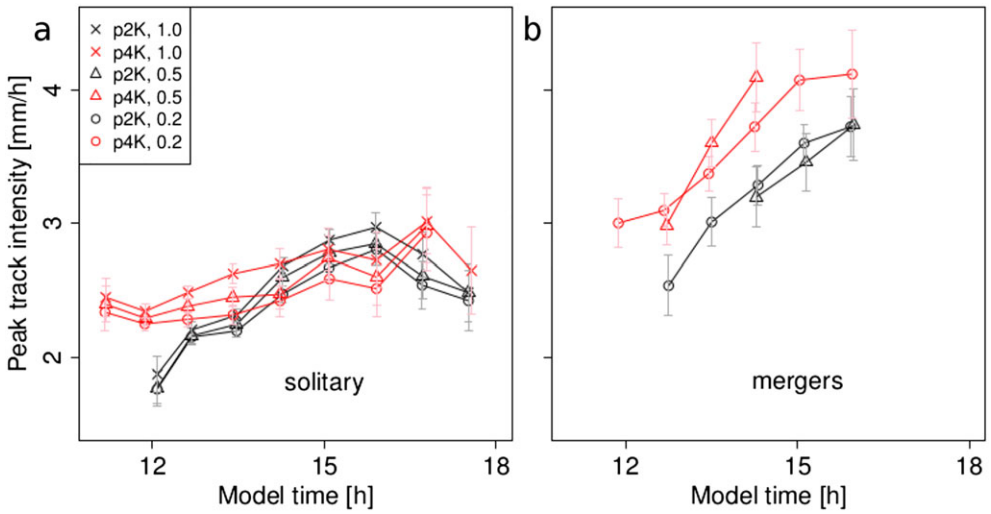

Figure 4. Peak track intensity versus time. Comparison of purely solitary (*s-s*) tracks (a) versus mergers (*m-a*) (b), for the simulations *P2K* and *P4K* (colors) and for termination sensitivities $\theta = 1.0$, $\theta = 0.5$, and $\theta = 0.2$ (symbols as shown in legend). Note that the case of $\theta = 1.0$ is not shown for merges in (b), since their number vanishes in this case. The error bars indicate the standard error for each data point.

$\theta = 1$, mergers completely vanish, as each track that a smaller tracks merges into is always continued and is considered as solitary (vice versa, in a fragmentation incident, the largest fragment always continues the original track). Therefore, in the case $\theta = 1$, the number of detected solitary tracks is maximal (see also supporting information section S1 for further details).

As an example, consider an instantaneous situation containing objects of all track types mentioned above (Figure 2). In this case, we use an intermediate value of $\theta = 0.5$, which allows the possibility of mergers. An example of a simulation with background large scale advection (OMEGA) is shown in Figure S1. To track rain cells in these data, the iteration feature of the tracking algorithm is applied. We contrast the advected with the unadvected *CTR* simulation at the same surface temperature. Figure 3 shows the corresponding total number of detected tracks, along with summary statistics, for each track type for the simulations, again for $\theta = 0.5$ to include mergers. Overall, tracks that are initiated as solitary are by far the most abundant. The second most prominent category is tracks originating as fragments or mergers but ending as solitary. Tracks both originating and ending as interaction incidents are relatively rare. Notably, when comparing the two simulations *P2K* and *P4K*, which have different surface temperature forcing T_0, stronger forcing leads to an increase of the number of mergers and fragmentations at the expense of the purely solitary tracks. The overall number of tracks remains nearly unaffected by the forcing change.

Mean track durations vary between 15 and 45 min and are largest for tracks originating as mergers. Shortest durations occur for tracks initiated and terminated as fragments—likely a statistical effect where multiple fragmentation processes take place in quick succession. As has been shown before (Moseley et al., 2016), under the forcing change, solitary tracks do not significantly change their duration, while tracks of all other categories do (mostly increasing for the stronger forcing).

The typical maximal spatial extent of tracks (quantified by $r_{\text{eff}} = \sqrt{A/\pi}$ where A is the maximum area that the track reaches) is 2–4 km and generally largest for tracks originating from merging. Merging not only leads to expectedly larger areas, but even the area average intensity of mergers increases relative to purely solitary tracks. Overall, the largest, and most intense, tracks result from repeated merging (*m-m*). Further, *m-m* tracks increase in number, duration, size, and intensity when the forcing is increased.

Together, these findings suggest that tracks involving some form of interaction (either merging or fragmentation) react to increased forcing. They do so by increasing duration, spatial extent, and precipitation intensity. Purely autonomous solitary tracks (i.e., of type *s-s*) show essentially no change in any of these properties. Furthermore, stronger forcing increases the probability of interference between tracks, a feature reflected by increased track numbers with merging or fragmentation, at the expense of purely solitary tracks. This

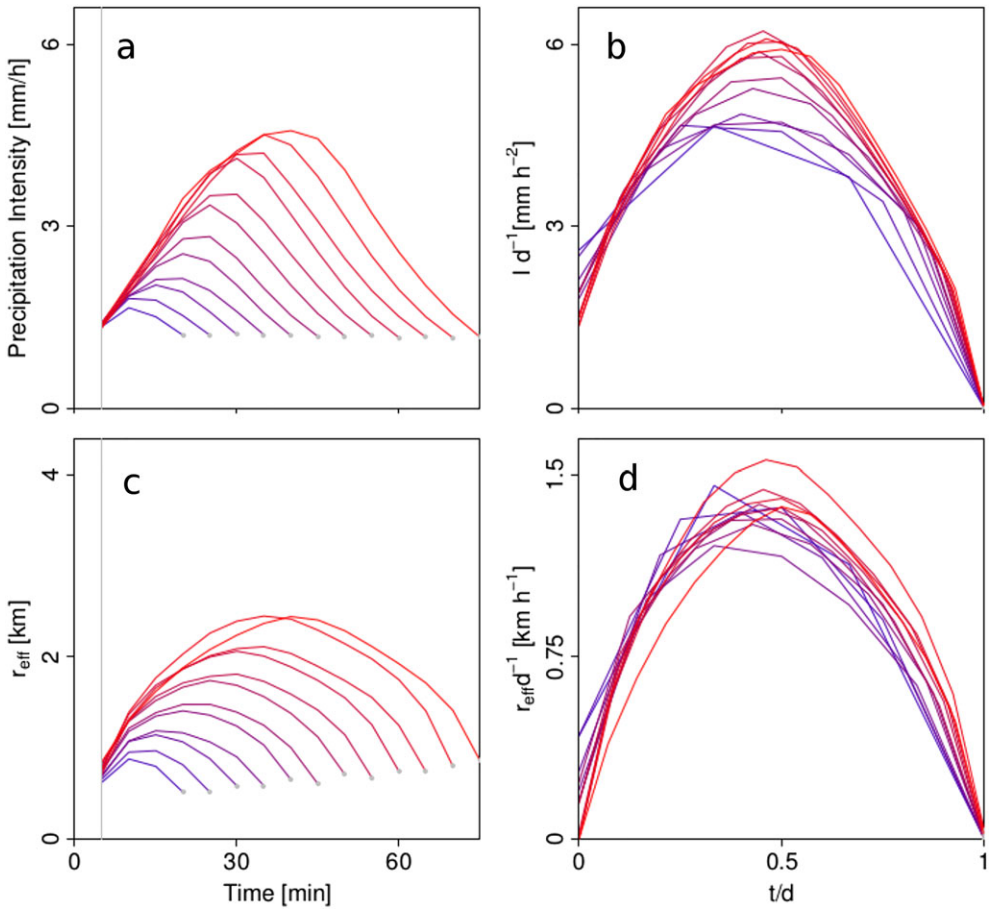

Figure 5. Time dependence across track duration. Precipitation intensity (a) and effective object radius (c) ($r_{\mathrm{eff}} \equiv \sqrt{A/\pi}$) versus time within tracks, for the P2K simulation and $\theta = 1.0$. Colors of curves indicate mean track life cycles conditioned on duration, ranging from 10 (blue) to 90 min (red). (b and d) Both axes normalized by total track duration. Intensity I is here defined as precipitation intensity minus the minimal intensity of the corresponding track average (typically the threshold intensity I_{min}).

shift, together with the aggravated properties of the interacting tracks, leads to overall more intense and more widespread domain-mean precipitation.

3.2. Time Evolution of Convective Rain Tracks

3.2.1. Evolution During the Diurnal Cycle

We find that track intensities steadily increase (with some noise) during the diurnal cycle (Figure 4). Hence, the longest duration and most intense tracks are expected in the late afternoon hours. The increase in duration is especially pronounced for mergers (type *m-a*), which indicates that longer and more intense tracks are formed by merging incidents during the course of the day. The intensification of mergers is more pronounced for stronger surface forcing (*P4K*). In addition, results are relatively robust against changes of the termination sensitivity θ between values of 0.2 and 1.0, especially for solitary tracks. However, mergers represent only a small fraction of the precipitation events, and thus in the following, we are mainly interested in the life cycles of solitary tracks and therefore choose $\theta = 1$, as the number of detected solitary tracks becomes largest in this case as stated above.

3.2.2. Track Life Cycles

We now consider how tracks evolve within their life cycles. As described previously (Moseley et al., 2016), solitary tracks show remarkably systematic properties: The mean temporal evolution of type *s-s* is characterized by a single-peaked structure in precipitation intensity, with the peak occurring approximately after half the track duration (Figure 5). We here find that the time dependence of precipitation intensity is closely mirrored by that of r_{eff}, where peaks also occur after approximately half the duration. When rescaling both

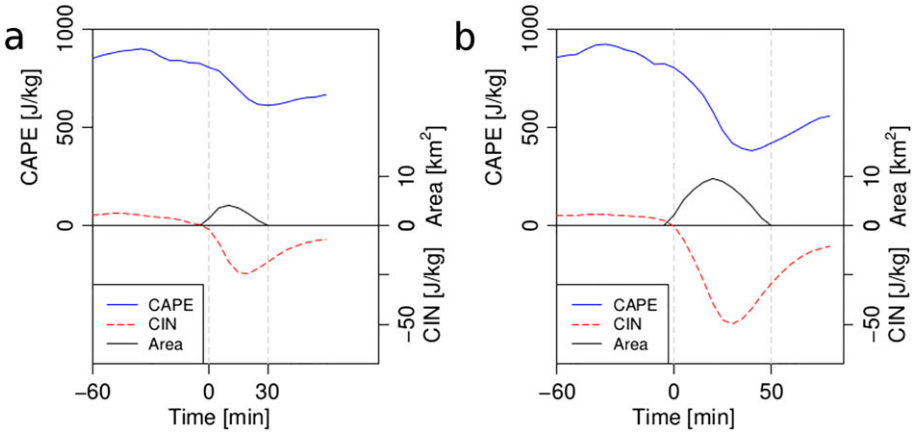

Figure 6. Mean CAPE life cycles. Mean track area, CAPE, and CIN (defined as negative values), over all solitary tracks with 30 min (a) and 50 min (b) life time, for the P2K simulation and $\theta = 1.0$. CAPE and CIN are given at the point of the track center of mass at the time of the maximum extent. Tracks begin at time $t = 0$; negative values of t show values before the onset of surface rain. CAPE = convective available potential energy; CIN = convective inhibition.

axes by the corresponding total track duration, all curves nearly collapse on one. This indicates that both the peak track intensity and peak cell diameter are approximately proportional to track duration.

Also, mergers show single-peaked life cycles (Figure S2). Precipitation intensity peaks are however generally higher and r_{eff} already has appreciable values at the beginning of these tracks—a feature that is not surprising, if it is considered that mergers are constituted by the concatenation of multiple solitary tracks at different, evolved, stages of their respective life cycles. As has already been discussed in Moseley et al. (2016), it is evident that both the initial precipitation intensity of mergers and the initial value of r_{eff} are elevated for the higher temperatures.

CAPE and CIN show very systematic behavior for purely solitary tracks (Figure 6): Independent of the track lengths, CAPE usually originates at very similar values (near 800 J/kg, a value within the range of typical values for observed convection; Jorgensen & Lemone, 1989) before precipitation onset and is only partially depleted within the track lifetime. The reason for CAPE starting at similar values independent of the size that the tracks reach is probably the similar atmospheric stratification for all events due to the absence of large scale forcing and advection. Therefore, the total amount of CAPE before the onset of a single convective event cannot be used as a predictor for the strength, size, and duration that it will reach.

In our results, CAPE rarely declines to zero after precipitation terminates. However, in some events, this is indeed the case (Figure S3). The consumption of CAPE might be hampered by precipitation itself which builds up CIN by cooling the lower boundary layer and thus prevents air to rise further. This finding speaks to a partial relaxation, where some CAPE remains. Only after precipitation ceases, CAPE slowly begins to recover. However, there is a clear relationship between the difference in CAPE at the beginning and the end of the tracks (termed ΔCAPE) and track duration—discussed further below. CIN, in turn, always originates near zero at precipitation onset and gradually builds up as the track continues (not shown). This does suggest CIN = 0 as a requirement for the onset of precipitation. Shorter tracks—those with smaller areas and intensities—end up with lower CIN than the longer ones, possibly due to enhanced evaporative cooling within the boundary layer as a consequence of stronger rain evaporation.

We note that CAPE and CIN strongly depend on the level that the air parcel is lifted from. In our case, this is the lowest model level which is strongly cooled by the cold pool that emerges as a result of rain evaporation. Therefore, a dominant reason for the rise in CIN and the depletion of CAPE immediately after the onset of surface rain is the marked drop in temperature, and potential reductions in humidity, in the lowest level caused by cold pools. A colder and drier air parcel experiences more negative buoyancy. In contrast, processes within the cloud layer, such as latent heating and mixing with the environment, have only a minor impact on local CAPE and CIN (see the vertical profiles of virtual potential temperature θ_v for a selected solitary track in Figure S3). To confirm the assumption that changes in CAPE and CIN are mainly driven by boundary layer processes, we calculated the quantities differently by substituting the horizontal mean profile of T_v into equations (1) and (2), instead of the local profiles at each column, and find only

small differences in the pattern (see Figure S4 for a horizontal snapshot). As most of the thermodynamic modification takes place in the lowest 500 m of the boundary layer where the test parcel is lifted from, but the background profile does not vary strongly further above, it does not matter much if CAPE or CIN are computed using a local profile or a horizontal mean profile. What does matter is that the test parcel is local.

A comparison of the time dependence for all four simulations CTR, P2K, P4K, and OMEGA (Figure S5) shows solitary track life cycles of intensity, temperature anomaly, and relative humidity. Again, the general picture is confirmed that for the three simulations CTR, P2K, and P4K, that is, in the absence of wind shear, solitary track life cycles are affected little (or not at all) by changes in surface forcing. The life cycles for OMEGA are clearly different from the other simulations, with weaker peaks in precipitation intensity, and nearly vanishing anomalies in near-surface temperature and relative humidity. This indicates that in the case of OMEGA, an analysis of CAPE or CIN is bound to be misleading. As we have shown, these buoyancy measures are mainly affected by the cooling and drying near the surface, which would then be displaced from the location of precipitation by the overall advection applied to this simulation. However, in the absence of wind shear, the emergent cold pool is clearly visible in the near surface temperature anomaly ΔT, which is systematically depressed after the onset of rain events (Figure S5). For longer-duration tracks, ΔT already recovers, while precipitation is still ongoing—an effect possibly due to (dryer and therefore warmer) downdrafts caused by decaying convection. We note that, upon termination of the track, the temperature anomaly is nearly identical for all track durations, $\Delta T \approx -.4K$. Relative humidity first increases (partially due to the decreases in temperature) but eventually becomes negative. The latter indicates a reduction also in specific humidity and could be explained by downdrafts, which bring relatively dry air down to the surface.

3.3. Linear Dependencies

An interesting picture emerges when studying the relation between several key quantities as they evolve throughout the tracks (Figure 7). To have a compact measure of precipitation intensity for each track, we define maximum event intensity as

$$I_{\max} \equiv max(I(t), t_i \leq t \leq t_f), \tag{4}$$

that is, simply as the maximum precipitation rate per unit area for all time steps during the track lifetime. As the plot shows, $I_{\max}$ scales all but linearly with the corresponding maximum effective event radius (defined analogously to equation (4)). A similarly linear relation is obtained when comparing the effective radius and track duration.

Together, these two plots further imply (not shown) that peak intensities scale roughly linearly with track duration: Short tracks of 10–20 min reach peak intensities of less than 2 mm/hr, while tracks that last 1 hr reach peaks of more than 4 mm/hr. CAPE, as a measure of integrated buoyancy, describes the atmosphere's ability of lifting an air parcel, usually involving that the parcel's water vapor condense during ascent. We compare CAPE to maximum effective event radius, finding again an approximately linear relationship (using maximum or average event intensity both give such near-linear dependencies). A similar linear relation holds for CIN. Hence, together,

$$\Delta CIN \sim \Delta CAPE \sim I_{\max}, \tag{5}$$

As already discussed above, both CAPE and CIN react to rain evaporation, which, at least at sufficiently short time scales, effectively shifts boundary layer temperatures proportional to the mass of rain evaporated. Indeed, if the tropopause temperature was constant during the track lifetime, and a change in surface temperature was linearly relaxed all the way up to the tropopause, and further assuming a boundary layer height of 1 km and tropopause height of $h = 15$ km, the change in CAPE would amount to

$$\Delta CAPE \approx g(h/2)\Delta T/T_{\text{ref}} \approx 200 \text{ J/kg}, \tag{6}$$

where $g = 9.81 \text{ ms}^{-2}$ and $\Delta T \approx 1$ K is assumed. However, longer tracks far exceed $\Delta CAPE \sim 200$J/Kg, while the temperature depression rarely exceeds 1.5K (Figure 7), suggesting that—at least in those cases—some of the change in potential energy is not due to boundary layer cooling alone.

As mentioned above, changes in CAPE are also due to humidity changes of a test parcel lifted from the surface (Figure 7). Relative humidity is generally enhanced for more intense events at approximately one

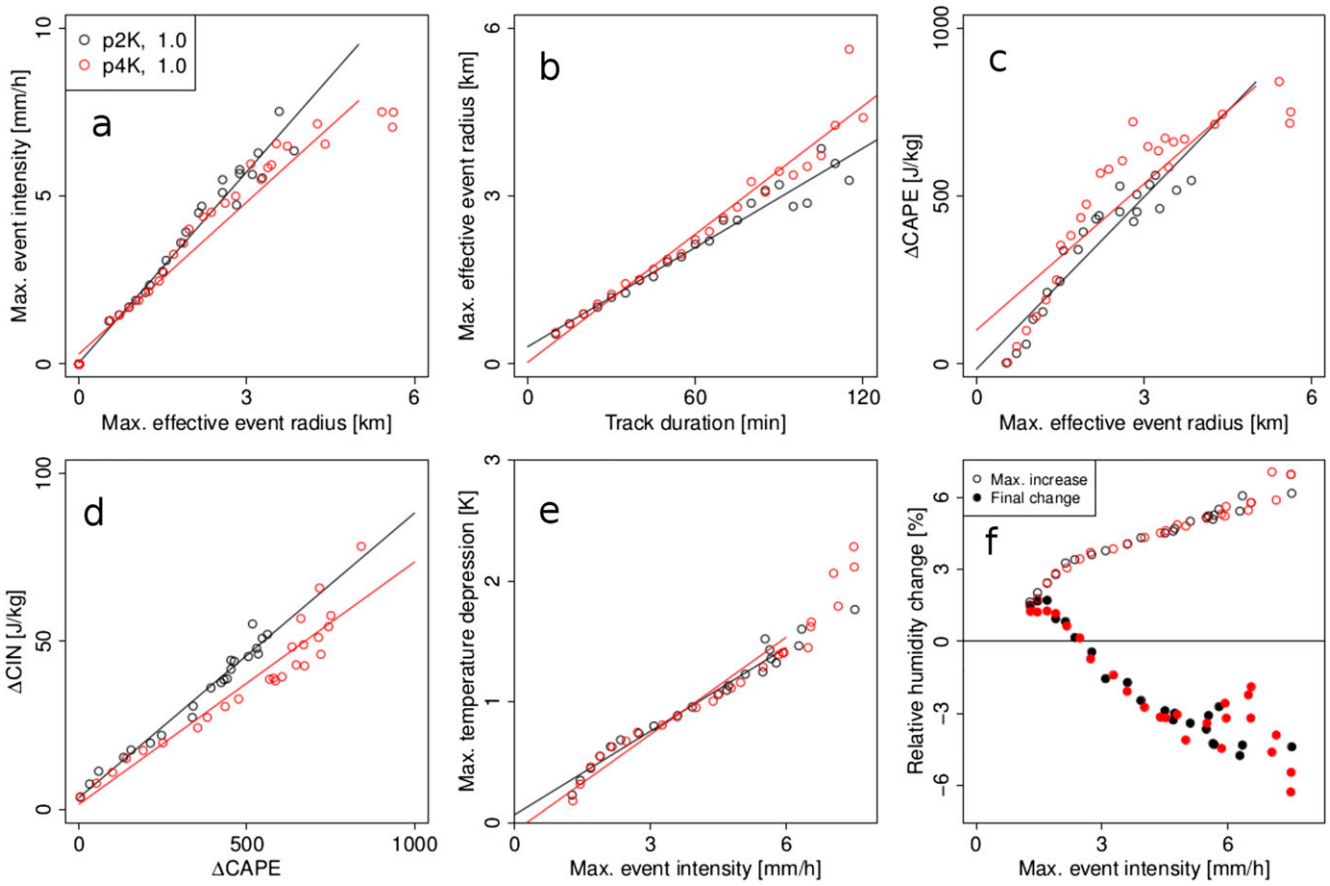

Figure 7. Various averaged relations for solitary tracks ($\theta = 1$). Panels show the relation of different parameters for solitary tracks, where each circle shows a mean value averaged over all solitary tracks of a given duration: maximum intensity versus maximum effective radius (a), maximum effective radius versus track duration (b), reduction in CAPE versus maximum effective radius (c), increase in CIN versus reduction in CAPE (d), maximum reduction in temperature versus maximum intensity (e), change in relative humidity versus maximum intensity (f). Gray lines are linear fits to the data corresponding to the four parameter choices. CAPE = convective available potential energy; CIN = convective inhibition.

third of the total track life time (Figure S5). Long tracks encounter increases of up to 4% during this time. Afterward, relative humidity decreases for all track lengths and is negative at the final track time step for long tracks (duration beyond 30 min). Indeed, relative humidity may play a key role in determining the thermodynamic structure of boundary layer air and its propensity for reaching positive buoyancy.

Considering the relative humidity change at the end of the track life cycles (Figure 7), reductions of 5% are not uncommon—drying that could result in significant increases in the LCL and thereby reductions in CAPE. Inspecting again Figure S3, one finds that near-surface virtual temperature has nearly recovered at the time when the precipitation event ends. However, the vertical temperature profile for a test parcel originating near the surface shows a substantial increase in the LCL (both relative to the LCL before precipitation onset and for a time of maximum event area). Hence, for events with large reductions in CAPE, boundary layer drying, not necessarily cloud layer heating, may be the main contribution.

3.4. A Statistical Model for Solitary Tracks

The previous discussion shows that solitary tracks have rather consistent properties, where the radius, intensity, and track lifetime are strongly linked. Consider therefore a simple geometric model for a precipitation track (Figure 8), where cells have a circular cross section and the intensity peaks at the center of this circle (where its value is I_0), and intensity decays linearly at a rate α that is similar for all cells:

$$I(r) = I_0 - \alpha r. \tag{7}$$

Further, cells are rotationally symmetric, that is, there is no azimuthal dependence of I. The geometric structure formed by (x, y, I) is hence a cone. The maximum radius of a cell is then determined by $I(r) = 0$;

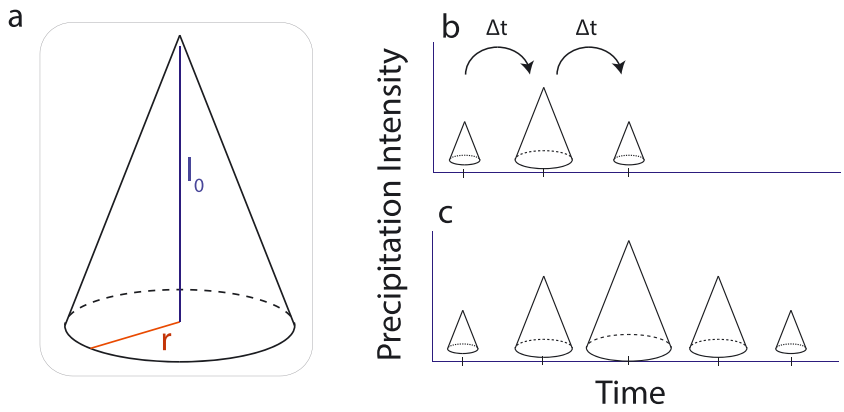

Figure 8. Cone model schematic. Cartoon image to the top right shows (a) the simple model for track intensity versus radius as a conal object in the space (x, y, I); (b) an example of a short track (consisting of three time steps); (c) a longer track (five time steps).

hence, $r_{\text{eff}} = I_0/\alpha$. Cell area $A(I_0)$, that is, the cross section projected onto the surface, is

$$A(I_0) = 2\pi r_{\max}^2 = 2\pi I_0^2/\alpha^2. \tag{8}$$

The spatially averaged cell intensity becomes

$$\bar{I}(I_0) = 2\pi/A(I_0) \int_{r=0}^{r_{\max}} \mathrm{d}r\, rI(r) = I_0/6. \tag{9}$$

Hence, indeed, cells with larger cross section radius would produce proportionately larger average intensities, that is, $\bar{I} \sim r_{\text{eff}}$. Further, knowing the average intensity, one also knows the maximum intensity—and vice versa. This is in line with the findings in other studies (Böing et al., 2012; Grabowski et al., 2006; Schlemmer & Hohenegger, 2014).

To check the validity of this simplified model, we build composites of objects of different areas. We average the intensity along circles around the center of mass of each object, while all grid boxes outside of each object's mask are assigned the value zero. Then, the resulting radial intensity profiles of all objects within the given area range are averaged. For solitary tracks, the resulting composite profiles are shown in Figure 9.

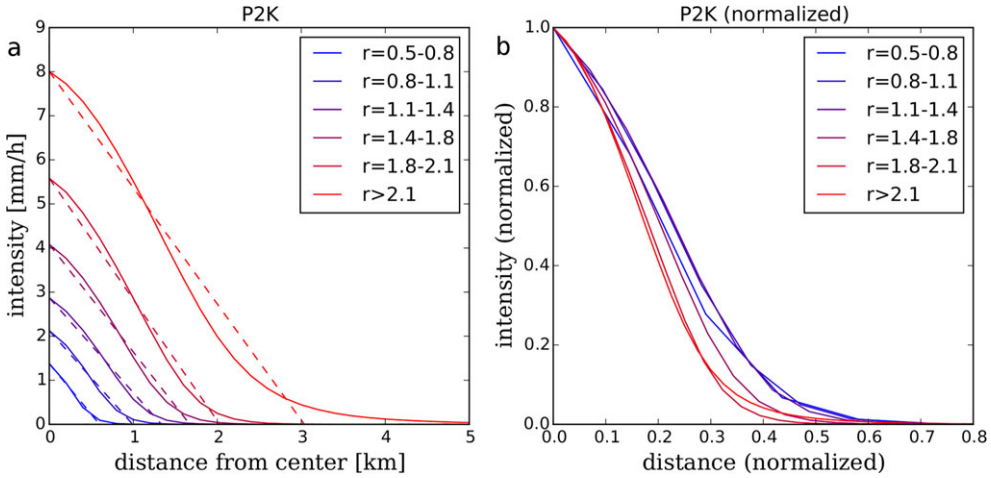

Figure 9. Radial precipitation intensity profiles. Mean precipitation intensity as a function of distance from the object center of mass, averaged over composites of all objects with similar effective radius r_{eff} (given in km), for the P2K simulation, and $\theta = 1$. (a) Absolute intensity versus distance from object mass center. Solid lines show averages over the object composites, dashed lines show fitted linear curves as given by equation (7). (b) Analogous but both axes scaled by the respective peak intensity, that is, the intensity in the object center of mass.

Table 1
Fitted Values for α From the Curves Shown in Figure 9 in Units of Millimeters per Hour per Kilometer

r_{max} (km)	0.5–0.8	0.8–1.1	1.1–1.4	1.4–1.8	1.8–2.1	>2.1
CTR ($\theta = 0.5$)	2.45	2.40	2.58	2.98	3.22	3.48
CTR ($\theta = 1.0$)	2.46	2.37	2.53	2.93	3.15	3.38
p2K ($\theta = 0.5$)	2.31	2.17	2.20	2.50	2.81	2.87
p2K ($\theta = 1.0$)	2.29	2.14	2.15	2.44	2.75	2.64
p4K ($\theta = 0.5$)	2.81	2.05	2.22	2.42	2.58	2.62
p4K ($\theta = 1.0$)	2.30	2.02	2.15	2.34	2.54	2.21

Even when the objects belonging to other track types are included, little difference in the results is seen (not shown). The long tails in contrast to the cone model can be explained by a small number of objects that have an elongated geometry, that is, they strongly deviate from a circular shape and thus have nonzero intensity also at larger distances (see Figure S6 for a schematic).

The linear dependencies (equation (7) and Figure 9) are fitted such that the averaged cell intensity given by equation (9) is equal to the one calculated from the respective profiles, when I_0 is taken as the peak intensity at $r = 0$. The fitted values for α are shown in Table 1 and vary between 2.14 and 2.75 for P2K and $\theta = 1$. Even the differences between the composites of *CTR*, *P2K*, and *P4K* and between the choices of $\theta = 0.5$, compared to $\theta = 1$, are rather moderate. However, there is a tendency for smaller values of α to occur in the case of stronger surface forcing (i.e., for P4K, in comparison to CTR and P2K), especially for larger cell sizes. This hints to more wide spread events in the case of stronger forcing. This assumption is supported by the fact that α is also smaller for $\theta = 1$, compared to $\theta = 0.5$, as in the former case, the solitary tracks are more contaminated by merging of smaller tracks. In conclusion, the simple linear model we propose here works sufficiently well. Although an exponentially decaying profile was suggested from a radar analysis by von Hardenberg et al. (2003), our simulated, idealized results here favor a linear profile. An advantage of a linear profile is a clearly defined spatial extent of the rain cells.

To shed more light on the spatial distribution of CAPE during the course of the tracks, in a similar way, we show composites of radial CAPE profiles, averaged over the beginning, the time of maximum extent, and the end of each solitary track (Figure 10), again conditioned on tracks of similar maximum effective radius r_{eff}. As a supplement to the time series shown in Figure 6, these radial profiles confirm that the original CAPE is only weakly disturbed at the onset of rain events but then reaches a strong depletion at the time of maximum track extent, especially toward the track center. When rain ceases, this strong depletion still remains and grows in extent.

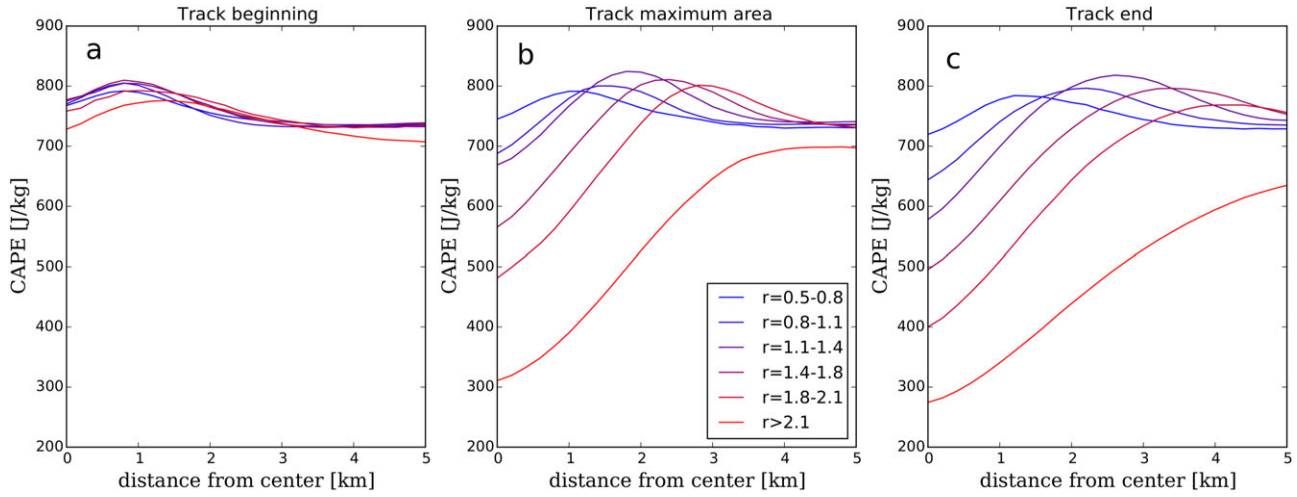

Figure 10. Radial profiles of CAPE. Mean CAPE as a function of distance from the object center of mass, averaged over composites of all tracks with similar maximum effective radius r_{eff}, for the P2K simulation, and $\theta = 1$. Mean profile at the initial time step of each track (a), at the time when each track reached its maximum extent (b), and at the last time step of each track (c). CAPE = convective available potential energy.

4. Conclusion and Outlook

We have shown that a simple rain cell tracking algorithm can elucidate a number of track properties and their relations. The tracking allows us to isolate the dynamics of tracks that begin and end autonomously, that is, without interference such as merging or fragmentation, so called solitary tracks. To avoid the termination of larger tracks that interact with smaller ones, we introduced a parameter θ that controls merging and splitting and show that the mean statistics of solitary tracks is relatively robust with respect to θ. For solitary tracks, we summarize our findings in a simple statistical model with spherically symmetric cells where the intensity falls of linearly with distance from the center (equation (7)). This model relates precipitation area, track lifetime, and precipitation intensity and gives a reasonable fit for solitary events of all sizes. Our findings imply that much of the initiation and termination of these isolated convective cells may be driven by processes occurring within the boundary layer—in particular, termination of convective updrafts may be mainly caused by cooling through rain reevaporation, rather than reductions in cloud level buoyancy.

It is remarkable, that, at least for the simple LES modeling setup without wind shear and homogeneous surface characteristics, solitary tracks follow systematic and relatively simple relations between the different quantities. This finding is encouraging, since, in this simple setup, there is hope for compressing the information on the cloud cell population into only few parameters. In particular, we have discussed the relation between several key parameters: the drop in CAPE and rise in CIN, the drop in near-surface temperature and humidity due to rain evaporation, and the track intensity. This relation indicates that, at least for a mean description of convective life cycles, one of these parameters is sufficient in predicting the others.

The current model is limited to the prediction of the mean properties of solitary precipitation life cycles. Future extensions of the model should address the full distribution of maximum intensities, or perhaps equivalently, the lifetimes of tracks. For an explanation of higher moments of the distribution of solitary track durations, more parameters might be required, like the total water content that has been identified as a crucial variable affecting moist convection (Derbyshire et al., 2004). Further, when wind shear is present, the presented simple model likely requires modifications.

We leave the question open if this picture could partially be carried over to merged tracks. When cells merge, they grow larger and, in qualitative agreement with the model we present, produce stronger precipitation intensities. Following this notion further, extreme convective precipitation may be a result of multiple, sequential merging incidents, resulting in very large precipitation areas and hence the largest intensities. These tracks (*m-m* type) are statistically rare but form the most intense precipitation, stemming from the largest cells with longest lifetimes. Incidentally, these *m-m* tracks intensify and grow further, as surface forcing is increased. Our findings support the previous claim that merging can invigorate precipitation intensity in tropical convective cells (Glenn & Krueger, 2017), as the interior of a merging object may be shielded against entrainment. Clouds can then become deeper due to the reduced entrainment and develop larger updraft velocities. Future work should however carefully assess, if the intensification is indeed *caused* by the merging process that can be explained, for example, by a "screening" effect where the interior of a merged cell suffers less from mixing processes, or if it is merely a statistical effect resulting from the fact that larger cells have a higher probability to merge into others.

Another crucial process in convective organization, not addressed here, is explicit triggering by cold pool dynamics, a topic currently discussed heavily in the community. Cold pool interactions, in distinction to merging processes, likely occur at larger spatial separation of the original precipitation cells. It has even been suggested that these scales are far from constant but may increase systematically in the course of the diurnal cycle—a possible consequence of the interplay of cold pool interaction (Haerter et al., 2018) and increasing CIN. Qualitatively revisiting the spatial pattern of the precipitation cell population in our simulations (Figure 2), cold pools are likely responsible for the clearing of several subareas of the model domain, most visible at $t - t_0 = 5$ hr for T_0 =25 °C. Such cold pool dynamics, which may act to widen the spatial buoyancy distribution, additionally increases the complexity of interactions and depletes the space available for precipitation cells to grow.

Future research in this area might benefit from a focus on processes facilitating repeated merging and the influence that cold pools might have on promoting or suppressing such merging. Fortunately, such processes, which often involve larger (6–8 km diameter) and longer lasting (30–40 min) tracks, may be measurable over vast regions of the globe through satellite data, which often can reach resolutions as high as 1.5–3 km spatially and ~15 min temporally.

Acknowledgments
C.M. acknowledges funding through the German Federal Ministry of Education and Research for the project "HD(CP)^2 - High definition clouds and precipitation for advancing climate prediction" within the framework programme "Research for Sustainable Development (FONA)," under 01LK1506F. J.O.H. and O.H. acknowledge funding through a grant (13168) by the Villum Foundation and the European Research Council (ERC) under the European Union's Horizon 2020 research and innovation program (grant agreement 771859). We acknowledge the German Climate Computing Center (DKRZ) for providing computing resources. The computer code for the UCLA-LES simulations is available at https://github.com/uclales. The computer code for the IRT tracking algorithm is available at https://github.com/christophermoseley/iterative_raincell_tracking. Other primary data and scripts that may by useful in reproducing the author's work are archived at DKRZ and are available at http://cera-www.dkrz.de/WDCC/ui/Compact.jsp?acronym=DKRZ_LTA_982_ds00001, or can be obtained by contacting publications@mpimet.mpg.de.

References

Arakawa, A. (2004). The cumulus parameterization problem: Past, present, and future. *Journal of Climate*, *17*(13), 2493–2525.

Arakawa, A., & Schubert, W. H. (1974). Interaction of a cumulus cloud ensemble with the large-scale environment, part I. *Journal of the Atmospheric Sciences*, *31*(3), 674–701.

Berg, P., Moseley, C., & Haerter, J. O. (2013). Strong increase in convective precipitation in response to higher temperatures. *Nature Geoscience*, *6*(3), 181–185.

Böing, S. J., Jonker, H. J., Siebesma, A. P., & Grabowski, W. W. (2012). Influence of the subcloud layer on the development of a deep convective ensemble. *Journal of the Atmospheric Sciences*, *69*(9), 2682–2698.

Byers, H. R., & Braham, R. R. (1949). *The thunderstorm: Report of the Thunderstorm Project*. Washington, DC: US Government Printing Office.

Dawe, J., & Austin, P. (2013). Direct entrainment and detrainment rate distributions of individual shallow cumulus clouds in an LES. *Atmospheric Chemistry and Physics*, *13*(15), 7795–7811.

Derbyshire, S., Beau, I., Bechtold, P., Grandpeix, J. Y., Pirou, J. M., Redelsperger, J. L., & Soares, P. (2004). Sensitivity of moist convection to environmental humidity. *Quarterly Journal of the Royal Meteorological Society*, *130*, 3055–3079. https://doi.org/0.1256/qj.03.130

Dixon, M., & Wiener, G. (1993). Titan: Thunderstorm identification, tracking, analsyis, and nowcasting—A radar-based methodology. *Journal of Atmospheric and Oceanic Technology*, *1993*, 785–797.

Done, J. M., Craig, G. C., Gray, S. L., Clark, P. A., & Gray, M. E. B. (2006). Mesoscale simulations of organized convection: Importance of convective equilibrium. *Quarterly Journal of the Royal Meteorological Society*, *132*(616), 737–756. https://doi.org/10.1256/qj.04.84

Emanual, K. A. (1994). *Atmospheric convection*. Oxford, UK: Oxford University Press.

Glenn, I., & Krueger, S. K. (2017). Connections matter: Updraft merging in organized tropical deep convection. *Geophysical Research Letters*, *44*, 7087–7094. https://doi.org/10.1002/2017GL074162

Grabowski, W. W., Bechtold, P., Cheng, A., Forbes, R., Halliwell, C., Khairoutdinov, M., et al. (2006). Daytime convective development over land: A model intercomparison based on LBA observations. *Quarterly Journal of the Royal Meteorological Society*, *132*(615), 317–344. https://doi.org/10.1256/qj.04.147

Haerter, J. O., Boeing, S. J., Henneberg, O., & Nissen, S. B. (2018). Reconciling cold pool dynamics with convective self-organization. https://arxiv.org/abs/1810.05518

Heiblum, R. H., Altaratz, O., Koren, I., Feingold, G., Kostinski, A. B., Khain, A. P., et al. (2016). Characterization of cumulus cloud fields using trajectories in the center of gravity versus water mass phase space: 1. Cloud tracking and phase space description. *Journal of Geophysical Research: Atmospheres*, *121*, 6336–6355. https://doi.org/10.1002/2015JD024186

Hering, A., Senesi, S., Ambrosetti, P., & Bernard-Bouissieres, I. (2005). Nowcasting thunderstorms in complex cases using radar data. In *WWRP Symbosium on Nowcasting and Very Short Range Forecasting, September 5th - 9th 2005, Toulouse* (pp. 2.14).

Heus, T., & Seifert, A. (2013). Automated tracking of shallow cumulus clouds in large domain, long duration large eddy simulations. *Geoscientific Model Development*, *4*, 1261–1273. https://doi.org/10.5194/gmd-6-1261-2013

Jorgensen, D. P., & Lemone, M. A. (1989). Vertical velocity characteristics of oceanic convection. *Journal of Atmospheric Sciences*, *46*, 621–640.

Kendon, E. J., Roberts, N. M., Fowler, H. J., Roberts, M. J., Chan, S. C., & Senior, C. A. (2014). Heavier summer downpours with climate change revealed by weather forecast resolution model. *Nature Climate Change*, *4*, 570–576.

Kober, K., & Tafferner, A. (2009). Tracking and nowcasting of convective cells using remote sensing data from radar and satellite. *Meteorologische Zeitschrift*, *18*(1), 75–84. https://doi.org/10.1127/0941-2948/2009/359

Lenderink, G., Barbero, R., Loriaux, J. M., & Fowler, H. J. (2017). Super-Clausius–Clapeyron scaling of extreme hourly convective precipitation and its relation to large-scale atmospheric conditions. *Journal of Climate*, *30*(15), 6037–6052. https://doi.org/10.1175/JCLI-D-16-0808.1

Lenderink, G., & van Meijgaard, E. (2008). Increase in hourly precipitation extremes beyond expectations from temperature changes. *Nature Geoscience*, *1*, 511–514.

Lenderink, G., van Meijgaard, E., & Selten, F. (2009). Intense coastal rainfall in the Netherlands in response to high sea surface temperatures: Analysis of the event of August 2006 from the perspective of a changing climate. *Climate Dynamics*, *32*, 19–33.

Lochbihler, K., Lenderink, G., & Siebesma, A. P. (2017). The spatial extent of rainfall events and its relation to precipitation scaling. *Geophysical Research Letters*, *44*, 8629–8636. https://doi.org/10.1002/2017GL074857

Molnar, P., Fatichi, S., Gaál, L., Szolgay, J., & Burlando, P. (2015). Storm type effects on super Clausius–Clapeyron scaling of intense rainstorm properties with air temperature. *Hydrology and Earth System Sciences*, *19*(4), 1753–1766.

Moseley, C., Berg, P., & Haerter, J. O. (2014). Probing the convection life-cycle by Iterative Rain Cell Tracking. *Journal of Geophysical Research: Atmospheres*, *118*, 13,361–13,370. https://doi.org/10.1002/2013JD020868

Moseley, C., Hohenegger, C., Berg, P., & Haerter, J. O. (2016). Intensification of convective extremes driven by cloud–cloud interaction. *Nature Geoscience*, *9*, 748–752.

Neelin, J. D., Peters, O., Lin, J. W. B., Hales, K., & Holloway, C. E. (2008). Rethinking convective quasi-equilibrium: Observational constraints for stochastic convective schemes in climate models. *Philosophical Transactions of the Royal Society of London A: Mathematical, Physical and Engineering Sciences*, *366*(1875), 2579–2602.

O'Gorman, P. A., & Schneider, T. (2009). Scaling of precipitation extremes over a wide range of climates simulated with an idealized GCM. *Journal of Climate*, *22*, 5676–5685.

Schlemmer, L., & Hohenegger, C. (2014). The formation of wider and deeper clouds as a results of cold-pool dynamics. *Journal of the Atmospheric Sciences*, *71*, 2842–2858.

Senf, F., Klocke, D., & Brueck, M. (2018). Size-resolved evaluation of simulated deep tropical convection. *Monthly Weather Review*, *146*(7), 2161–2182. https://doi.org/10.1175/MWR-D-17-0378.1

Simpson, J., Westcott, N. E., Clerman, R., & Pielke, R. (1980). On cumulus mergersüber das verschmelzen von cumulus-wolken. *Archiv für Meteorologie, Geophysik und Bioklimatologie, Serie A*, *29*(1-2), 1–40.

Stevens, B., Stevens, B., Moeng, C.-H., Ackerman, A. S., Bretherton, C. S., Chlond, A., et al. (2005). Evaluation of large-eddy simulations via observations of nocturnal marine stratocumulus. *Monthly Weather Review*, *133*(6), 1443–1462.

Tao, W. K., & Simpson, J. (1989). A further study of cumulus interactions and mergers: Three-dimensional simulations with trajectory analyses. *Journal of the Atmospheric Sciences*, *46*(19), 2974–3004.

Tsai, W. M., & Wu, C. M. (2017). The environment of aggregated deep convection. *Journal of Advances in Modeling Earth Systems*, *9*, 2061–2078. https://doi.org/10.1002/2017MS000967

von Hardenberg, J., Ferraris, L., & Provenzale, A. (2003). The shape of convective rain cells. *Geophysical Research Letters*, *30*(24), 2280. https://doi.org/10.1029/2003GL018539

Westra, S., Fowler, H., Evans, J., Alexander, L., Berg, P., Johnson, F., et al. (2014). *Reviews of Geophysics*, *52*, 522–555. https://doi.org/10.1002/2014RG000464

Zimmer, M., Craig, G. C., Keil, C., & Wernli, H. (2011). Classification of precipitation events with a convective response timescale and their forecasting characteristics. *Geophysical Research Letters*, *38*, L05802. https://doi.org/10.1029/2010GL046199